Revision 1 Word Count: 6613

Revision 1

The new mineral tomiolloite, $Al_{12}(Te^{4+}O_3)_5[(SO_3)_{0.5}(SO_4)_{0.5}](OH)_{24}$: a unique microporous tellurite structure

OWEN P. MISSEN[1,2,*], STUART J. MILLS[1], MICHAEL S. RUMSEY[3], JOHN SPRATT[4], JENS NAJORKA[4], ANTHONY R. KAMPF[5] AND BRENT THORNE[6]

[1]Geosciences, Museums Victoria, GPO Box 666, Melbourne 3001, Victoria, Australia

[2]School of Earth, Atmosphere and Environment, Monash University, Clayton 3800, Victoria, Australia

[3]Department of Earth Sciences, Natural History Museum, Cromwell Road, London SW7 5BD, England, UK

[4]Department of Core Research Laboratories, Natural History Museum, Cromwell Road, London SW7 5BD, England, UK

[5]Mineral Sciences Department, Natural History Museum of Los Angeles County, 900 Exposition Boulevard, Los Angeles, CA 90007, USA

[6]3898 Newport Circle, Bountiful, UT 84010, USA

*Corresponding e-mail: omissen@museum.vic.gov.au

New mineral tomiolloite: a unique microporous tellurite

ABSTRACT

Tomiolloite (IMA2021-019) is a new aluminium tellurite sulfite–sulfate mineral discovered at the Bambolla mine, Moctezuma, Sonora, Mexico, a well-known tellurium (Te) mineral locality. Tomiolloite forms roughly spherical clusters of crystals comprised of very thin, needle-like crystals (1 μm diameter, ~40 μm length) around a core of small, stubbier, broken crystals. Tomiolloite is generally found growing on tellurite or quartz. The strongest powder X-ray diffraction lines are [d_{obs}Å(I_{obs})(*hkl*)]: 11.667(89)(100), 8.240(38)(101), 4.107(29)(202,211,121), 3.223(100)(203,302,130) and 2.905(37)(213,123,222,400). The empirical formula of tomiolloite, as determined by electron microprobe analysis, is $(Al_{10.64}Te^{6+}_{1.01}Fe^{3+}_{0.31}Zn_{0.04})_{\Sigma 12}(Te^{4+}_{5.00}Pb_{0.02})_{\Sigma 5.02}(S^{4+}_{0.49}S^{6+}_{0.49}Si_{0.02})_{\Sigma 1.00}O_{21.53}[(OH)_{20.86}Cl_{0.11}]_{\Sigma 20.97}$, which is simplified to the ideal formula $Al_{12}(Te^{4+}O_3)_5[(SO_3)_{0.5}(SO_4)_{0.5}](OH)_{24}$. Significant Te^{6+} substitution for Al^{3+} is observed in tomiolloite, verified by X-ray photoelectron spectroscopy and crystal structure analysis. The structure of tomiolloite was determined using Synchrotron single-crystal X-ray diffraction, showing that tomiolloite is hexagonal and crystallizes in the space-group $P6_3/m$, with the unit cell parameters a = 13.3360(19) Å, c = 11.604(2) Å, V = 1787.3(6) Å^3 and Z = 2. Tomiolloite has a unique microporous framework structure, which bears a slight similarity to that of zemannite, but it has a much larger cavity diameter (8.85 Å). The framework is built from edge-sharing $M\varphi_6$ octahedra (M = Al^{3+} and Te^{6+}), $Te^{4+}O_3$ trigonal pyramids and $Te^{4+}O_4$ disphenoids. $M\varphi_6$ octahedra edge-share to form crankshaft-shaped chains along c, with $Te^{4+}O_n$ polyhedra filling notches in the crankshafts and providing linkages between adjacent chains. The framework has an overall positive charge, which is balanced by the presence of both sulfite (SO_3^{2-}) trigonal pyramids and sulfate (SO_4^{2-}) tetrahedra in the channels.

Keywords: new mineral; crystal structure; tellurium oxysalt; microporous; Synchrotron radiation; Moctezuma, Sonora, Mexico

INTRODUCTION

Tomiolloite is a new aluminium tellurite sulfite–sulfate mineral with the ideal formula $Al_{12}(Te^{4+}O_3)_5[(SO_3)_{0.5}(SO_4)_{0.5}](OH)_{24}$, adding to the rich chemical and structural diversity of tellurium (Te) oxysalt minerals (Christy et al. 2016a). The most common cations in Te oxysalt minerals are Pb^{2+} and/or Cu^{2+}, while relatively few Te oxysalts contain additional anions, such as sulfate or carbonate (Christy et al. 2016b). Tomiolloite, however, contains Al^{3+} as its main cation, and for the first time amongst Te oxysalts, the sulfite anion is present as an additional anion, along with sulfate. In fact, tomiolloite is only the third sulfite–sulfate mineral to be described, after orschallite, $Ca_3(SO_3)_2(SO_4)\cdot 12H_2O$ (Wiedenthaler et al. 1993) and hielscherite, $Ca_3Si(SO_4)(SO_3)(OH)_6\cdot 11H_2O$ (Pekov et al. 2012). Additionally, tomiolloite is the third Al–Te oxysalt mineral to be described, and the other two both contain at least one other metallic cation. Burckhardtite $[Pb^{2+}_2(Fe^{3+}Te^{6+})(AlSi_3O_8)O_6]$ was also described from the Bambolla mine (Gaines 1979; Christy et al. 2014), while backite ($Pb^{2+}_2AlTe^{6+}O_6Cl$) was identified from the Grand Central mine, Tombstone, Arizona (Tait et al. 2015). Al–Te–O materials are also studied as non-crystalline solids, such as erbium-doped aluminium tellurite glass for light emission (Brovelli *et al*. 2007). However, Al–Te oxysalts are a little-studied class of materials (Table 1) and it is likely that further analysis of both crystalline and non-crystalline samples will result in the description of new structures or materials with potentially interesting properties.

The name and formula of tomiolloite (IMA2021-019) have been approved by the Commission on New Minerals Nomenclature and Classification (CNMNC) of the International Mineralogical Association (IMA) (Missen et al. 2021). Tomiolloite is named for the Nahuatl word for 'fuzzy' ('*tomiollo*') in allusion to the appearance of near-spherical clusters of tomiolloite crystals. Nahuatl is the language of the Nahua peoples who live in the Moctezuma area, continuing a naming tradition used for Moctezuma secondary minerals (e.g.

tlalocite and xocomecatlite, Williams 1975; cuzticite and eztlite, Williams 1982; xocolatlite, Grundler et al. 2008). The holotype specimen of tomiolloite is deposited in the collections of Museums Victoria, Melbourne, Australia, with specimen number M55489.

OCCURRENCE AND PARAGENESIS

Tomiolloite occurs at the Bambolla mine (aka Moctezuma mine), Moctezuma, Sonora, Mexico (29.69169°N, 109.71220°W). Further descriptions of the mineral assemblages found at the locality are provided in many papers (e.g. Gaines 1970; Rewitzer and im Wald 2001; Grundler et al. 2008). Tomiolloite is the 26th new mineral to be described from the mines near Moctezuma, of which 22 are Te oxysalts. Most of these Te oxysalts were identified between 1960 and 1980, the first worldwide occurrence of a diverse assemblage of Te oxysalts (Gaines, 1970; Grundler et al. 2008). The specimen used to define tomiolloite as a new mineral was collected in February 1999 by one of the authors (BT) from the dumps around the main shaft. The white spheres were later identified growing on tellurite (Figs. 1 and 2) under an optical microscope.

Associated minerals

The holotype specimen of tomiolloite contains only two other minerals: quartz and tellurite (TeO_2), the latter forming coarse, rough crystals up to 3 mm in length. Tomiolloite is found coating both quartz and tellurite in different areas of the specimen.

During our investigations of Moctezuma mine specimens, abundant white ‘fluffy’ crusts and isolated spheres were identified coating tellurite and mroseite (Mandarino et al., 1975) on Natural History Museum specimen BM 1974,394 (Fig. 3). Their identity was verified as tomiolloite during this study by powder X-ray diffraction. Further investigation might have led to the identification of tomiolloite many decades ago, exemplifying herein the

99 importance of thoroughly studying and revisiting complex and unusual assemblages in
100 museum collections acquired contemporaneously with new mineral descriptions.
101
102 **Origin of the mineral**
103 Tomiolloite and other secondary Te minerals at Moctezuma are believed to have
104 formed from oxidation of primary tellurium and/or telluride phases. The Al^{3+} in tomiolloite
105 was probably produced from the weathering of K-feldspar, a common rock-forming mineral
106 in the rhyolite prevalent at Bambolla. The occurrence of tomiolloite on tellurite suggests that
107 it is formed by late-stage alteration of primary minerals, perhaps in a second generation of
108 secondary alteration. Neither primary Te minerals nor K-feldspar (or another possible source
109 for the Al^{3+}) are present on the tomiolloite specimen, suggesting that tomiolloite forms either
110 (1) spatially separated from its parent minerals following aqueous transport or (2) its parent
111 minerals are fully dissolved in the oxidizing environment that produces tomiolloite.
112
113 **APPEARANCE, PHYSICAL AND OPTCIAL PROPERTIES**
114 Tomiolloite forms nearly spherical aggregates of very thin needles, resulting in a
115 white 'puffball' appearance. It is found growing on quartz or tellurite (Fig. 1). Individual
116 puffballs are generally no more than 100 μm in diameter, averaging 50 μm, composed of
117 hair-like individual needles with diameters rarely exceeding 1 μm (Fig. 2) and lengths rarely
118 exceeding 40 μm. The centers of the puffballs are formed around nuclei of stubbier
119 microcrystals of tomiolloite (<5 μm). No forms could be determined and twinning was not
120 observed. Tomiolloite has a white streak and pearly luster. It does not fluoresce under short-
121 wave ultraviolet light. The hardness was not determinable due to the thinness of the needles,
122 although the Mohs hardness is likely to be < 3. Neither cleavage nor parting was observed.

Tomiolloite has a brittle tenacity and uneven fracture, with a calculated density of 3.374 g/cm^3. The official IMA symbol (Warr 2021) for tomiolloite is *Toi*.

Optical properties of tomiolloite were difficult to determine due to the thinness of the needles. Tomiolloite is uniaxial (–). n_{ave} was calculated from the Gladstone-Dale compatibility index as 1.762 using the room-temperature PXRD unit cell. ω and ε were calculated as 1.79(1) and 1.71(1) respectively from n_{ave} after measuring the γ–α birefringence [0.08(1), using a Bertrand lens and a 530 nm gypsum plate]. Tomiolloite exhibits faint pleochroism, with *O* greyish-blue and *E* brownish-yellow with $E > O$.

Infrared (IR) Spectroscopy

IR spectroscopy was conducted on a Bruker Alpha FTIR with a diamond Attenuated. Total Reflectance attachment (ATR), DTGS (Deuterated Triglycine Sulfate) detector, 4 cm^{-1} resolution and 4000–450 cm^{-1} range. The samples were placed on the ATR crystal and pressure exerted by screwing the pressure clamp onto the sample to ensure maximum contact with the ATR crystal. Thirty-two scans were taken for each item and co-added.

The IR spectrum of a crushed tomiolloite aggregate (Fig. 4) shows the presence of the tellurite anion $(Te^{4+}O_3)^{2-}$ and both the sulfite $(SO_3)^{2-}$ and sulfate $(SO_4)^{2-}$ anions. The two peaks at 775 and 693 cm^{-1} may be attributed to the tellurite anion, slightly higher than the typical values for tellurite IR peaks observed in other tellurite minerals, which often fall between 635 and 700 cm^{-1} (Pekov et al. 2011). The splitting of the 775 cm^{-1} peak may be related to the presence of minor tellurate $(Te^{6+}O_6)^{6-}$ substitution in the structure (see below). In the S–O region, the spectrum displays similarities to the IR spectrum of the mixed sulfite–sulfate mineral hielscherite (Pekov et al. 2012). Both hielscherite and tomiolloite have a composite peak with shoulder peaks on either side corresponding the major sulfite and sulfate anions. In tomiolloite, the notable peaks are found at 921 cm^{-1} (sulfite), 1007 cm^{-1}

(composite) and 1164 cm^{-1} (sulfate). Between 4000 and 1400 cm^{-1}, the only major peak in the tomiolloite IR spectrum is a small peak centered on 3626 cm^{-1} attributable to OH. No bands corresponding to H_2O were observed.

X-ray Photoelectron Spectroscopy (XPS)

XPS was conducted using a Nexsa Surface Analysis System at the Monash X-ray Platform (MXP) of Monash University, Clayton, Australia and data were processed using Avantage software (both by Thermo Fisher Scientific). X-rays were generated with a Mg target producing K_α radiation with a beam size of 100 μm. The binding energy scale was referenced to amorphous C1*s* at 284.5 eV. A full-range spectrum was collected first before collecting detailed scans in the S2*p* (160–177 eV; Fig. 5a) and Te3*d* regions (560–600 eV; Fig. 5b).

The XPS spectrum in the Te region shows two peaks, both of which were fitted with two curves. The major peaks at 576.4 and 586.8 correspond to $3d_{5/2}$ and $3d_{3/2}$ peaks of species-forming Te^{4+}, respectively (compared with the reference compound TeO_2 with Te^{4+} peaks at 576.3 and 586.7; Thermo Fisher 2013–2021). The shoulder peaks at 577.3 and 587.7 correspond to $3d_{5/2}$ and $3d_{3/2}$ peaks of minor Te^{6+} (compared with the reference compound $Ca_{10}Na_{10}[Te_9O_{42}](H_2O)$ with Te^{6+} peaks at 577.5 and 587.5; Zhang & Lii 2019).

Despite low signal to noise ratio for S, the presence of both S^{4+} and S^{6+} in tomiolloite was confirmed. The broad peak from 166 to 171 eV encompasses peaks of both S^{4+} (166–168.5 eV) and S^{6+} (167.5–170 eV). The S^{4+} reference compound Na_2SO_3 has $2p_{3/2}$ and $2p_{1/2}$ peaks at 166.5 and 167.6 (Thermo Fisher 2013–2021). The S^{6+} reference compound Na_2SO_4 has $2p_{3/2}$ and $2p_{1/2}$ peaks at 168.5 and 169.6 (Thermo Fisher 2013–2021).

CHEMISTRY

Quantitative chemical spot analyses (5) of a small fragment removed from the tomiolloite holotype specimen and mounted in a probe block were performed on a Cameca SX100 electron microprobe (WDS mode, 20 kV, 20 nA, 1 μm beam diameter and PAP matrix correction) at the Imaging and Analysis Centre, Core Research Laboratories, NHM. The X-ray lines and standards used for element determination were: Al*K*α – corundum, S*K*α – barite, Cl*K*α – halite, Fe*K*α – hematite, Zn*K*α – sphalerite, Te*L*α – Bi_2Te_3 and Pb*M*α – vanadinite. Na_2O, MgO, CaO, V_2O_5, MnO, CuO, As_2O_5 and Bi_2O_3 were sought, but not detected. The analytical data are presented in Table 2.

The empirical formula based on $(Al^{3+}+Te^{6+}+Fe^{3+}+Zn^{2+})$ = 12 *pfu* is $(Al_{10.64}Te^{6+}_{1.01}Fe^{3+}_{0.31}Zn_{0.04})_{\Sigma 12}(Te^{4+}_{5.00}Pb_{0.02})_{\Sigma 5.02}(S^{4+}_{0.49}S^{6+}_{0.49}Si_{0.02})_{\Sigma 1.00}O_{21.53}[(OH)_{20.86}Cl_{0.11}]_{\Sigma 20.97}$. H_2O was calculated based on the crystal structure which indicated 42.5 O+OH anions *pfu*. The simplified formula is $(Al,Te^{6+},Fe^{3+},Zn)_{12}(Te^{4+},Pb)_5(S^{4+},S^{6+})O_{18.5}[(OH),O,Cl]_{24}$ and general formula is $[Al_{12-x}Te^{6+}_x](Te^{4+}O_3)_5(OH)_{24-3x}O_{3x}[(SO_3)_{0.5}(SO_4)_{0.5}]$. The holotype sample of tomiolloite has $x \approx 1$ and the endmember formula has $x = 0$. The ideal endmember formula is $Al_{12}(Te^{4+}O_3)_5[(SO_3)_{0.5}(SO_4)_{0.5}](OH)_{24}$ which requires Al_2O_3 36.03, TeO_2 47.00, SO_2 1.89, SO_3 2.36, H_2O 12.73, total 100 wt.%.

CRYSTALLOGRAPHY

X-ray powder diffraction

A puffball of tomiolloite crystals was removed from the holotype specimen (M55489) and attached to a non-diffracting amorphous-carbon fiber (10 μm diameter) glued to a glass support rod. This sample was mounted on a Rigaku Rapid II micro-diffractometer at the Natural History Museum, London, and a dataset was collected using Cu*K*α radiation (40 kV and 36 mA). Diffraction data were collected at ambient temperature using a 300 μm beam

collimator, a primary graphite monochromator and a 2D curved image plate detector. A Gandolfi-type randomized sample movement was achieved by rotations on the φ and ω axes. The 2D diffraction data were converted to 1D patterns using the 2DP software (Rigaku). Observed d_{hkl} and reflection intensities were derived by profile-fitting using Highscore Plus software (Panalytical), although the dataset used was truncated at 60º 2θ due to poorly defined, low-intensity reflections at higher angles. High background resulted in lower-than-expected relative intensities for reflections found at less than 20° 2θ (d_{obs} greater than 4.46; see Table 3).

The unit-cell parameters of tomiolloite were refined using Chekcell (Laugier & Bochu 2004) from the powder data and are a = 13.355(2) Å, c = 11.614(2) Å and V = 1793.9(6) Å^3. These parameters are in good agreement with the SXRD unit cell and with the pattern calculated from the structure using the PowderCell program (Kraus and Nolze 1996).

Single Crystal X-ray Diffraction

Single crystal X-ray diffraction data were collected on the micro-focus macromolecular MX2 beamline at the Australian Synchrotron, part of ANSTO (Aragao et al. 2018). A 1 × 1 × 30 μm transparent needle of tomiolloite was selected from the holotype specimen. Data were collected at 100(1) K by a Dectris EigerX 16M detector using monochromatic radiation with a wavelength of 0.71096 Å.

Reflection intensities were integrated, corrected for Lorentz and polarization effects, and converted to structure factors using the program CrysalisPro® (Rigaku Oxford Diffraction), finding 32626 reflections with an R_{int} of 0.0945. Absorption correction was performed by multi-scan SADABS (Bruker, 2001). Structure solution was carried out using SHELXS-97 (Sheldrick 2008), followed by structural refinement using full-matrix least-squares implemented by SHELXL-2018/3 (Sheldrick 2015), using neutral atomic scattering

222 factors. The asymmetric unit of the structure contains three Te sites (including the split
223 occupancy Te2), two Al-dominant *M* sites, one S site and 11 O/OH sites (including the split
224 occupancy O2). The occupancies for Te and O in the two mixed sites were allowed to refine
225 freely, converging to Te2A:Te2B of 0.732:0.268(4) and O2A:O2B of 0.54:0.46(7).
226 Additionally, free-variable refinements on the *M* sites led to the values 1.064(12) and
227 1.021(13). These values were used to constrain Te^{6+} occupancies in the *M* sites (as
228 determined by EPMA and analysis of Te:Al ratios, further discussed below).

229 Reflections with calculated F_{obs}/F_{calc} errors greater than 5.00 were omitted from the
230 final refinement. All atom positions and anisotropic displacement parameters (U^{ij}) for all
231 atoms except the split site O2 and atoms in SO_3 trigonal pyramids were refined to final R_1
232 and wR_2 (all data) values of 0.0808 and 0.1784, respectively. Further details of data collection
233 and structure refinement are provided in Supplementary Table S1. A summary of bond
234 lengths is provided in Table 4 and a bond-valence analysis is provided in Table 5, using the
235 parameters of Mills and Christy (2013) for Te–O bonds and Gagné and Hawthorne (2015) for
236 all other bonds.

237 Crystallographic data for tomiolloite in the form of the Crystallographic Information
238 File (CIF) been deposited with the Cambridge Crystallographic Data Centre, CCDC, 12
239 Union Road, Cambridge CB21EZ, UK. Copies of the data can be obtained free of charge on
240 quoting the depository number CSD-2115386 (Fax: +44-1223-336-033; E-Mail:
241 deposit@ccdc.cam.ac.uk, http://www.ccdc.cam.ac.uk). The CIF is also available in the
242 supplementary online material for this article.

243

244 **Crystal-Structure Description**

245 The crystal structure of tomiolloite is a microporous framework with a channel
246 diameter of 8.85 Å (Fig. 6), built from edge-sharing $M\varphi_6$ octahedra (M = Al^{3+} and Te^{6+}),

247 $Te^{4+}O_3$ trigonal pyramids and $Te^{4+}O_4$ disphenoids. The $M\varphi_6$ octahedra each edge-share with
248 three adjacent octahedra to form crankshaft-shaped infinite chains along *c* (Fig. 7). Each
249 chain links to three others *via* corner-sharing, creating a channel which is filled by $Te1^{4+}O_3$
250 trigonal pyramids, bonded to the chains by both primary and secondary linkages (Te–O bonds
251 <2.7 Å and >2.7 Å, respectively; Christy & Mills, 2013). The Te2 site is split across two
252 locations 0.819(4) Å apart (Fig. 8), nestled into the notches in the crankshaft chains. The
253 refined occupancy of Te2A:Te2B is 0.732:0.268(4). The Te2A location is a trigonal pyramid,
254 sharing two O3 sites with the $M1\varphi_6$ octahedra and an isolated O2 site, which is strongly
255 bonded to Te2A. The three strongly bonded O sites of Te2B (O3 ×2 and O4) are all shared
256 with the chains, while the fourth O (O2) is more distantly bonded, forming a strongly
257 distorted [3+1] disphenoidal coordination. The O2 site is also split across two positions,
258 0.56(3) Å apart (Fig. 8), leading to two orientations of the Te2A trigonal pyramid and Te2B
259 disphenoid. The O2B site forms an unusually short (strong) bond of 1.72(3) Å to Te2A.
260 The *M* sites are Al^{3+} dominant but also contain minor Te^{6+}, confirmed by XPS (see
261 Fig. 5b). Refining free variables on the two Al-dominant sites showed an excess of electrons
262 for both sites (with the excess three times greater for the Al1 site compared to the Al2 site),
263 suggesting the substitution of small amounts of a heavier atom (i.e. Te^{6+}) for Al^{3+}. The Te^{6+}
264 was split across the two sites in a 3:1 ratio leading to an overall Al:Te ratio of 11:6 in the
265 crystal structure, matching the EPMA. The presence of Te^{6+} in the Al^{3+} sites leads to an
266 elevated bond-valence for the O sites bonded to the octahedra, allowing for a charge-balance
267 OH→O substitution mechanism and the general formula
268 $[Al_{12-x}Te^{6+}_x](Te^{4+}O_3)_5(OH)_{24-3x}O_{3x}[(SO_3)_{0.5}(SO_4)_{0.5}]$. This substitution is likely to occur *via*
269 the O4 site, which contributes 3 O atoms *pfu* of tomiolloite and can undergo (OH→O)
270 substitution. In the structure refinement of tomiolloite, the bond-valence of the O4 site is 1.36
271 *vu*, leading to the assignment of O and overall $O_{18}(OH)_{21}$ in the framework ($x\approx1$). The

valence of the O4 site drops to 1.22 *vu* without Te^{6+}, leading to the assignment of OH and overall framework $O_{15}(OH)_{24}$ ($x \approx 0$).

Overall, the microporous framework has the formula $[(Al_{11}Te^{6+}_{1})_{\Sigma 12}(Te^{4+}O_3)_5O_3(OH)_{21}]^{2+}$. The positive charge is offset by the presence of SO_3 and SO_4 anions in the channels. Although the crystal structure shows only SO_3 trigonal pyramids (Fig. 9), the IR spectrum indicates the presence of SO_4 and XPS indicates the presence of S^{6+} in tomiolloite. The bond-valence for the three S–O bonds averages 1.41 *vu*, approximately halfway between the expected bond-valence for O in a SO_3 group (1.33 *vu*) and SO_4 group (1.50 *vu*). Each S and associated O1S and O2S sites have an occupancy of 0.31(3). Despite the ideal formula having exactly ⅓ occupancy of the S site, fixing the occupancy of S and associated O led to unreasonably high displacement parameters. The occupancy of the tetrahedral apex O is expected to be 0.15(2), with an assumed 1:1 ratio of SO_3:SO_4. Fixing the SO_3:SO_4 ratio at 1:1, represented by $[(SO_3)_{0.5}(SO_4)_{0.5}]$ in the structural formula, is reasonable as the data does not show dominance of either S oxyanion. Practically, the approach we take with tomiolloite is consistent with numerous zeolitic minerals which have multiple different species within their channels but are defined as one mineral, such as bosoite [$SiO_2 \cdot nC_xH_{2x+2}$; Momma et al. 2020], lazurite [$Na_6Ca_2(Al_6Si_6O_{24})(SO_4,S,S_2,S_3,Cl,OH)_2$; Tauson et al. 2012] and melanophlogite [$46SiO_2 \cdot 2M^{12} \cdot 6M^{14}$, in which molecules such as CH_4, N_2, CO_2 and H_2S occupy the two cage types in the structure; e.g. Kanzaki 2019]. The putative tetrahedral apex O site would correspond to only 1 e^- in the difference Fourier map, which we cannot observe given the quality of the data obtained from a thin needle. H-atoms also cannot be observed due to high difference peaks and troughs. OH sites were assigned based on the bond-valence and a tentative H-bonding network may be developed using the O···O distances (see Table 5).

297 **Relationship to other minerals**

298 Tomiolloite has a unique chemical composition amongst natural compounds and is
299 only the third Te oxysalt mineral to also contain Al, after burckhardtite (Christy et al. 2014)
300 and backite (Tait et al. 2015). Burckhardtite and backite both contain additional metallic
301 cations whereas Al^{3+} is the only metallic cation in tomiolloite. Burckhardtite is also notable
302 for a shared site of octahedral Te^{6+} and Fe^{3+}, as opposed to Te^{6+} and Al^{3+} in tomiolloite. One
303 synthetic Al–Te–S–O–H compound $[Al_2(Te^{4+}O_3)(SO_4)(OH)_2]$ has previously been
304 synthesized and is the closest chemical relative to tomiolloite (Johansson & Lindqvist 1976).
305 In general, Al–Te–O compounds are not a well-studied group of compounds, with the full list
306 of six known crystalline Al–Te–O compounds provided in Table 1.

307 Chemically, the presence of both SO_3^{2-} and SO_4^{2-} anions in tomiolloite is also
308 unusual. Just two other minerals contain statistical SO_3^{2-} and SO_4^{2-}: orschallite (Wiedenthaler
309 et al. 1993) and hielscherite (Pekov et al. 2012), both of which contain Ca^{2+} as the major
310 metallic cation. The presence of both S^{4+} and S^{6+} in the one structure requires basic
311 conditions in which kinetic, rather than thermodynamic, factors dominate as usually S^{4+}
312 oxidizes fully to S^{6+} (Choudhary et al., 2015). It is worth noting that other SO_x^{y-} anions occur
313 in Te–O minerals e.g. SO_4^{2-} in adanite (Kampf et al. 2020a) and the rare thiosulfate ($S^{6+}O_3S^{2-}$
314) anion in northstarite (Kampf et al., 2020b), but tomiolloite is the first Te–O mineral to
315 contain the sulfite anion. Despite the thermodynamic instability of the sulfite anion, other
316 SO_3^{2-} minerals such as scotlandite ($PbSO_3$) may also be found on mine dumps (Paar et al.,
317 1984).

318 Structurally, tomiolloite shares some similarities with the microporous tellurite
319 zemannite (Missen et al. 2019) and the isotypic minerals keystoneite (Missen et al. 2021),
320 kinichilite (Koyama & Nagashima 1981; Miletich 1995) and ilirneyite (Pekov et al. 2018).
321 Like zemannite, tomiolloite contains isolated *neso* tellurite $(Te^{4+}O_3)^{2-}$ groups, which are

incorporated into a larger structural group (Christy et al. 2016a) by MO$_6$ octahedra, where M is a metallic cation. In all other facets, the structures are divergent. The arrangement of the MO$_6$ octahedra in the two structure types is significantly different, leading to a negatively charged framework in the zemannite structure and a positively charged framework in tomiolloite. Tomiolloite also contains $Te^{4+}O_4^{4-}$ disphenoids in the split (Te2) site. Consequently, the channels in zemannite are occupied by hydrated Mg^{2+} cations whereas in tomiolloite the channels are occupied by SO_3^{2-} and SO_4^{2-} anions.

IMPLICATIONS

As a technology-critical metal for emerging areas such as solar panels, it remains remarkable how little the surface geochemistry of tellurium is understood (Filella et al. 2019). Tellurium bonding and chemical behavior is highly versatile due to the availability of several oxidation states (Chivers & Laitinen 2015). A better understanding of Te geochemical behavior in surface environments is required due to its increasing anthropogenic usage (Missen et al. 2020), of which a key aspect is characterizing the wide variation in chemistry, structure and paragenesis of secondary tellurium minerals to understand the behavior of Te in the weathering environment.

Weathering gold- and copper-bearing deposits are the natural 'playground' for tellurium environmental geochemistry. Tellurium is present in most of its oxidation states (-2 to 0 in primary minerals, +4 and +6 once oxidized) in these environments. The Moctezuma mining area, and the Bambolla mine in particular, showcases the weathering of a native tellurium-rich ore (Grundler et al. 2008). It is notable that most of the secondary Te minerals at the Bambolla deposit, including tomiolloite, are tellurite (Te^{4+}) minerals, while at other Te mineral localities such as Otto Mountain, California, USA, the Pb–Cu–Te mineralogy is largely comprised of tellurate (Te^{6+}) minerals (Christy et al. 2016b). Whether the reason for this dichotomy is due to the prevailing weathering conditions or chemistry of the local

environment is not well-understood. Otto Mountain's main primary mineral is the silver telluride hessite rather than native tellurium, reflecting differences in the original ore forming fluids (Brugger et al. 2016). Understanding these mineralogical aspects of tellurium surface chemistry will provide valuable clues for managing the behavior of Te in anthropogenically enriched areas, such as solar panel stockpiles and Cu-mining tailings piles.

ACKNOWLEDGEMENTS

This study has been partly funded by The Ian Potter Foundation grant 'tracking tellurium' to SJM. Microprobe work was funded through Natural Environment Research Council grant NE/M010848/1 'Tellurium and Selenium Cycling and Supply' to Chris J. Stanley (Natural History Museum, London). Support funding has also been provided to OPM by an Australian Government Research Training Program (RTP) Scholarship, a Monash Graduate Excellence Scholarship (MGES) and a Robert Blackwood Monash–Museums Victoria scholarship. We acknowledge Joël Brugger (Monash University) for his insightful comments and PhD supervision of OPM. This research was undertaken in part using the MX2 beamline at the Australian Synchrotron, part of ANSTO, and made use of the Australian Cancer Research Foundation (ACRF) detector.

REFERENCES CITED

Aragao, D., Aishima, J., Cherukuvada, H., Clarken, R., Clift, M., Cowieson, N.P., Ericsson, D.J., Gee, C.L., Macedo, S., Mudie, N., Panjikar, S., Price, J.R., Riboldi-Tunnicliffe, A., Rostan, R., Williamson, R. and Caradoc-Davies, T.T. (2018) MX2: a high-flux undulator microfocus beamline serving both the chemical and macromolecular crystallography communities at the Australian Synchrotron. Journal of Synchrotron Radiation, 25, 885-891.

Brovelli, S., Galli, A., Lorenzi, R., Meinardi, F., Spinolo, G., Tavazzi, S., Sigaev, V., Sukhov, S., Pernice, P. and Aronne, A. (2007) Efficient 1.53 μm erbium light emission in heavily Er-doped titania-modified aluminium tellurite glasses. Journal of non-crystalline solids, 353, 2150-2156.

Brugger, J., Liu, W., Etschmann, B., Mei, Y., Sherman, D.M. and Testemale, D. (2016) A review of the coordination chemistry of hydrothermal systems, or do coordination changes make ore deposits? Chemical Geology, 447, 219-253.

Bruker (2001) SADABS and XPREP. Bruker AXS Inc., Madison, WI, USA.

Choudhary, L., Macdonald, D.D. and Alfantazi, A. (2015) Role of thiosulfate in the corrosion of steels: a review. Corrosion, 71, 1147-1168.

Chivers, T. and Laitinen, R.S. (2015) Tellurium: a maverick among the chalcogens. Chemical Society Reviews, 44, 1725-1739.

Christy, A.G. and Mills, S.J. (2013) Effect of lone-pair stereoactivity on polyhedral volume and structural flexibility: application to $Te^{IV}O_6$ octahedra. Acta Crystallographica, B69, 446–456.

Christy, A.G., Kampf, A.R., Mills, S.J., Housley, R.M. and Thorne, B. (2014) Crystal structure and revised chemical formula for burckhardtite, $Pb_2(Fe^{3+}Te^{6+})[AlSi_3O_8]O_6$: a double-sheet silicate with intercalated phyllotellurate layers. Mineralogical Magazine, 78, 1763-1773.

Christy, A.G., Mills, S.J., and Kampf, A.R. (2016a) A review of the structural architecture of tellurium oxycompounds. Mineralogical Magazine, 80, 415–545.

Christy, A.G., Mills, S.J., Kampf, A.R., Housley, R.M., Thorne, B. and Marty, J. (2016b) The relationship between mineral composition, crystal structure and paragenetic sequence: the case of secondary Te mineralization at the Bird Nest drift, Otto Mountain, California, USA. Mineralogical Magazine, 80, 291-310.

Filella, M., Reimann, C., Biver, M., Rodushkin, I. and Rodushkina, K. (2019) Tellurium in the environment: current knowledge and identification of gaps. Environmental Chemistry, 16, 215-228.

Gagné, O.C. and Hawthorne, F.C. (2015) Comprehensive derivation of bond-valence parameters for ion pairs involving oxygen. Acta Crystallographica, B71, 562–578.

Gaines, R.V. (1970) The Moctezuma tellurium deposit. Mineralogical Record, 1, 40-43.

Gaines, R.V. (1979) Burckhardtite, a new silicate-tellurite from Mexico. American Mineralogist, 64, 355-358.

Grundler, P.V., Brugger, J., Meisser, N., Ansermet, S., Borg, S., Etschmann, B., Testemale, D. and Bolin, T. (2008) Xocolatlite, $Ca_2Mn^{4+}{}_2(Te^{6+}O_6)_2 \cdot H_2O$, a new tellurate related to kuranakhite: description and measurement of Te oxidation state by XANES spectroscopy. American Mineralogist, 93, 1911-1920.

Johansson, G. and Lindqvist, O. (1976) The crystal structure of $Al_2(OH)_2TeO_3SO_4$. Acta Crystallographica, B32, 407-411.

Kampf, A.R., Housley, R.M., Rossman, G.R., Yang, H. and Downs, R.T. (2020a) Adanite, a new lead-tellurite-sulfate mineral from the North Star mine, Tintic, Utah, and Tombstone, Arizona, USA. Canadian Mineralogist, 58, 403-410.

Kampf, A.R., Housley, R.M. and Rossman, G.R. (2020b) Northstarite, a new lead-tellurite-thiosulfate mineral from the North Star mine, Tintic, Utah, USA. Canadian Mineralogist, 58, 533-542.

Kanzaki, M. (2019) High–temperature Raman spectroscopic study of CO2–containing melanophlogite. Journal of Mineralogical and Petrological Sciences, 114, 122-129.

Koyama, E. and Nagashima, K. (1981) Kinichilite, a new mineral from the Kawazu mine, Shimoda city, Japan. Mineralogical Journal, 10, 333-337.

Kraus, W. and Nolze, G. (1996) POWDER CELL—a program for the representation and manipulation of crystal structures and calculation of the resulting X-ray powder patterns. Journal of Applied Crystallography, 29, 301–303.

Laugier, J. and Bochu, B. (2004) Chekcell: Graphical powder indexing cell and space group assignment software, http://www.ccp14.ac.uk/tutorial/lmgp/.

Li, P.-F., Kong, F. and Mao, J.-G. (2020) $M^{II}{}_2M_3{}^{III}F_3(Te_6F_2O_{16})$ (M^{II} = Pb, Ba; M^{III} = Al, Ga): New mixed anionic tellurites with isolated Te_6 coplanar rings. Journal of Solid State Chemistry, 286, 121288.

Miletich, R. (1995) Crystal chemistry of the microporous tellurite minerals zemannite and kinichilite, $Mg_{0.5}[Me^{2+}Fe^{3+}(TeO_3)_3]\cdot 4.5H_2O$, ($Me^{2+}$=Zn;Mn). European Journal of Mineralogy, 7, 509-524.

Mandarino, J.A., Mitchell, R.S. and Hancock, R.G.V. (1975) Mroseite, a calcium tellurite-carbonate from Moctezuma, Sonora, Mexico. Canadian Mineralogist, 13, 286-288.

Mills, S.J. and Christy, A.G. (2013) Revised values of the bond-valence parameters for Te^{IV}–O, Te^{VI}–O and Te^{IV}–Cl. Acta Crystallographica, B69, 145–149.

Missen, O.P., Mills, S.J., Spratt, J., Birch, W.D. and Brugger, J. (2019) Crystal chemistry of zemannite-type structures: I. A re-examination of zemannite from Moctezuma, Mexico. European Journal of Mineralogy, 31, 519-527.

Missen, O.P., Ram, R., Mills, S.J., Etschmann, B., Reith, F., Shuster, J., Smith, D.J. and Brugger, J. (2020) Love is in the Earth: a review of tellurium (bio)geochemistry in surface environments. Earth-Science Reviews, 204, 103150.

Missen, O.P., Back, M.E., Mills, S.J., Roberts, A.C., LePage, Y., Pinch, W.W. & Mandarino, J.A. (2021) Keystoneite, the Ni^{2+}-analogue of zemannite, and ferrotellurite discredited. Canadian Mineralogist, 59, 1-10.

Missen, O.P., Mills, S.J., Rumsey, M.S., Spratt, J., Najorka, J., Kampf, A.R. and Thorne, B. (2021) Tomiolloite, IMA 2021-019. CNMNC Newsletter 62, European Journal of Mineralogy, 33, https://doi.org/10.5194/ejm-33-479-2021.

Momma, K., Ikeda, T., Nagase, T., Kuribayashi, T., Honma, C., Nishikubo, K., Takahashi, N., Takada, M., Matsushita, Y., Miyawaki, R. and Matsubara, S. (2020) Bosoite, a new silica clathrate mineral from Chiba Prefecture, Japan. Mineralogical Magazine, 84, 941-948.

Paar, W., Braithwaite, R., Chen, T. and Keller, P. (1984) A new mineral, scotlandite ($PbSO_3$) from Leadhills, Scotland; the first naturally occurring sulphite. Mineralogical Magazine, 48, 283-288.

Pekov, I.V., Chukanov, N.V., Zadov, A.E., Roberts, A.C., Jensen, M.C., Zubkova, N.V. and Nikischer, A.J. (2011) Eurekadumpite, $(Cu,Zn)_{16}(TeO_3)_2(AsO_4)_3Cl(OH)_{18}\cdot 7H_2O$, a new supergene mineral species. Geology of Ore Deposits, 53, 575-582.

Pekov, I., Chukanov, N., Britvin, S., Kabalov, Y.K., Göttlicher, J., Yapaskurt, V., Zadov, A., Krivovichev, S., Schüller, W. and Ternes, B. (2012) The sulfite anion in ettringite-group minerals: a new mineral species hielscherite, $Ca_3Si(OH)_6(SO_4)(SO_3)\cdot 11H_2O$, and the thaumasite–hielscherite solid-solution series. Mineralogical Magazine, 76, 1133-1152.

Pekov, I.V., Siidra, O.I., Vlasov, E.A., Yapaskurt, V.O., Polekhovsky, Y.S. and Apletalin, A.V., (2018) Ilirneyite, $Mg_{0.5}[ZnMn^{3+}(TeO_3)_3]\cdot 4.5H_2O$, a New Mineral from Chukotka, Russia. Canadian Mineralogist, 56, 1-9.

Rewitzer, C. and im Wald, F. (2001): Bambolla, Bambollita, San Miguel und Candelaria: Untertage-Funde und Typmineralien von Moctezuma. Lapis, 26, 24-40.

Sheldrick, G.M. (2008) A short history of *SHELX*. Acta Crystallographica, A64, 112-122.

Sheldrick, G.M. (2015) Crystal structure refinement with *SHELXL*. Acta Crystallographica, C71, 3–8.

Tait, K.T., DiCecco, V., Ball, N.A., Hawthorne, F.C., and Kampf, A.R. (2015) Backite, $Pb_2Al(TeO_6)Cl$, a new tellurate mineral from the Grand Central mine, Tombstone Hills, Cochise County, Arizona: description and crystal structure. Canadian Mineralogist, 52, 935–942.

Tauson, V.L., Goettlicher, J., Sapozhnikov, A.N., Mangold, S. and Lustenberg, E.E. (2012) Sulphur speciation in lazurite-type minerals $(Na,Ca)_8[Al_6Si_6O_{24}](SO_4,S)_2$ and their annealing products: a comparative XPS and XAS study. European Journal of Mineralogy, 24, 133-152.

Thermo Fisher Scientific Inc. (2013-2021) Sulfur. Accessed from https://xpssimplified.com/elements/sulfur.php on 29 January 2021.

Thermo Fisher Scientific Inc. (2013-2021) Tellurium. Accessed from https://xpssimplified.com/elements/tellurium.php on 29 January 2021.

Warr, L.N. (2021) IMA–CNMNC approved mineral symbols. Mineralogical Magazine, 85, 291–320.

Weidenthaler, C., Tillmanns, E. and Hentschel, G. (1993) Orschallite, $Ca_3(SO_3)_2SO_4\cdot 12H_2O$, a new calcium-sulfite-sulfate-hydrate mineral. Mineralogy and Petrology, 48, 167-177.

Williams, S.A. (1975) Xocomecatlite, $Cu_3TeO_4(OH)_4$, and tlalocite, $Cu_{10}Zn_6(TeO_3)(TeO_4)_2Cl(OH)_{25}\cdot 27H_2O$, two new minerals from Moctezuma, Sonora, Mexico. Mineralogical Magazine, 40, 221-226.

Williams, S.A. (1982) Cuzticite and eztlite, two new tellurium minerals from Moctezuma, Mexico. Mineralogical Magazine, 46, 257-259.

Zhang, L.-Y. and Lii, K.-H. (2019) $Ca_{10}Na_{10}[Te_9O_{42}](H_2O)$: a hydrothermally synthesized quaternary tellurium(VI) oxide containing edge-sharing octahedral trimers. Dalton Transactions, 48, 15231-15235.

This is the peer-reviewed, final accepted version for American Mineralogist, published by the Mineralogical Society of America.
The published version is subject to change. Cite as Authors (Year) Title. American Mineralogist, in press.
DOI: https://doi.org/10.2138/am-2022-8368. http://www.minsocam.org/

TABLES

Table 1: Al–Te–O minerals and related synthetic compounds (shown in chronological order of description/synthesis)

Mineral	Formula	Symmetry and space-group	Year described	Comment	Type locality / synthesis	Reference(s)
			Minerals			
Burckhardtite	$[Pb^{2+}_2(Fe^{3+}Te^{6+})(AlSi_3O_8)O_6]$	Trigonal, $P\bar{3}1m$	1979	Only secondary Te silicate	Moctezuma, Mexico	Gaines (1979); Christy et al. (2014)
Backite	$Pb^{2+}_2AlTe^{6+}O_6Cl$	Trigonal, $P312$	2015	Unique chemical composition	Tombstone, Arizona	Tait et al. (2015)
Tomiolloite	$Al_{12}(Te^{4+}O_3)_5[(SO_3)_{0.5}(SO_4)_{0.5}](OH)_{24}$	Hexagonal, $P6_3/m$	2021	First Al–Te^{4+}–O mineral	Moctezuma, Mexico	This study
			Synthetic compounds			
NA	$Al_2(Te^{4+}O_3)(SO_4)(OH)_2$	Monoclinic, $P2_1/m$	1976	First Al–Te–O compound	Hydrothermal	Johansson & Lindqvist (1976)
NA	$Na_3[(Fe^{3+}_{1.5}Al_{1.5})(Te^{6+}O_6)_2]$	Cubic, $Ia\bar{3}d$	1999	Garnet structure tellurate	Solid-state reaction	Wedel and Sugiyama (1999)
NA	$Pb_2Al_3F_3(Te^{4+}_6F_2O_{16})$	Tetragonal, $P4/mbm$	2020	Contains unique fluoride-tellurite ring	Hydrothermal	Li et al. (2020)

499 **Table 2:** EPMA data for holotype tomiolloite

	Holotype specimen (M55489) (5 analyses)		
Oxide wt%	Average	Range	St. Dev.
Al_2O_3	**29.69**	28.71–30.79	0.88
SiO_2	**0.08**	0.05–0.12	0.03
SO_2*	**1.71**	1.59–1.83	0.09
SO_3*	**2.14**	1.98–2.28	0.11
Cl	**0.22**	0.18–0.33	0.06
Fe_2O_3	**1.36**	0.77–2.10	0.56
ZnO	**0.17**	0.11–0.20	0.03
TeO_2*	**43.65**	41.08–45.48	1.60
TeO_3*	**9.78**	6.91–11.98	1.99
PbO	**0.28**	0.15–0.39	0.10
H_2O*	**10.29**	28.71–30.79	0.88
O=Cl	**-0.05**	0.05–0.12	0.03
Total	**99.32**		

500 *H_2O calculated based on 42.5 O+OH anions *pfu*, assuming a 1:1 ratio of $(SO_3)^{2-}$:$(SO_4)^{2-}$ and
501 $(Al^{3+}+Te^{6+}+Fe^{3+}+Zn^{2+}) = 12$

Table 3. X-ray powder diffraction data (*d* in Å) for tomiolloite. The five strongest lines are highlighted in bold. Cutoff: averaged $I > 5$, $d > 1.5$.

I_{meas}	d_{meas}	*h k l*	I_{calc}	d_{calc}	I_{meas}	d_{meas}	*h k l*	I_{calc}	d_{calc}
89	**11.667**	**1 0 0**	**100**	**11.549**			1 1 4	2	2.660
38	**8.240**	**1 0 1**	**12**	**8.188**	15	2.669	2 3 0	1	2.650
14	5.807	1 1 1	7	5.781			3 2 0	2	2.650
		2 0 0	5	5.775	21	2.593	3 2 1	5	2.583
20	5.204	1 0 2	9	5.185			2 3 1	4	2.583
		1 1 2	8	4.377	7	2.529	1 4 0	2	2.520
29	4.395	1 2 0	2	4.365			4 1 0	2	2.520
		2 1 0	1	4.365	17	2.322	4 0 3	3	2.314
		2 0 2	**6**	**4.093**			4 1 2	3	2.312
29	**4.107**	**2 1 1**	**9**	**4.086**	11	2.157	2 0 5	1	2.153
		1 2 1	**2**	**4.086**			1 3 4	1	2.150
10	3.670	3 0 1	4	3.654			0 0 6	1	1.934
31	3.503	2 1 2	2	3.488	7	1.932	3 3 3	1	1.927
		1 2 2	10	3.488			6 0 0	2	1.925
18	3.349	2 2 0	5	3.334			1 4 4	3	1.903
		2 0 3	**27**	**3.213**	19	1.908	2 4 3	2	1.901
100	**3.223**	**3 0 2**	**7**	**3.208**			4 2 3	2	1.901
		1 3 0	**2**	**3.203**	12	1.835	2 0 6	2	1.834
12	3.102	1 3 1	7	3.088			5 1 3	1	1.828
		2 1 3	**8**	**2.895**			2 5 1	1	1.826
37	**2.905**	**1 2 3**	**2**	**2.895**	10	1.812	5 2 1	1	1.826
		2 2 2	**2**	**2.891**			5 0 4	3	1.807
		4 0 0	**3**	**2.887**			4 3 2	1	1.805
9	2.820	3 1 2	2	2.804			3 2 5	2	1.750
		4 0 1	1	2.802	14	1.752	2 3 5	1	1.750
9	2.739	3 0 3	2	2.729			2 4 4	1	1.744
					12	1.678	2 2 6	4	1.673

Table 4. Selected bond lengths for tomiolloite

Te1–O1 (×3)	1.899(5)	*M*1–O5	1.870(5)	S-O2S	1.50(3)
Te1–O3 (×3)	2.531(6)	*M*1–O6	1.873(5)	S-O1S (×2)	1.51(3)
<Te1–O>	**2.215**	*M*1–O7	1.889(5)	**<S–O>**	**1.51**
		*M*1–O1	1.902(5)		
Te2A–O2B	1.72(3)	*M*1–O4	1.905(5)	O···O	distances
Te2A–O3 (×2)	1.851(5)	*M*1–O8	2.008(5)	O2A–O8	2.552
Te2A–O2A	1.890(18)	**<*M*1–O>***	**1.908**	O2A–O2S	3.091
Te2A–O4	2.971(8)			O2B–O8	2.661
Te2A–O1S (×2)	3.29(9)	*M*2–O5	1.843(5)	O2B–O2S	2.575
$<Te2A–O>_{short}$	**1.828**	*M*2–O3	1.862(6)	O5–O1S	3.119
$<Te2A–O>_{long}$	**2.996**	*M*2–O7	1.868(5)	O6–O1S	3.174
		*M*2–O1	1.894(5)	O6–O7	3.300
Te2B–O3 (×2)	1.944(6)	*M*2–O8	1.927(5)	O7–O1S	3.173
Te2B–O4	2.164(8)	*M*2–O8	1.988(5)		
Te2B–O2B	2.52(3)	**<*M*2–O>***	**1.897**		
Te2B–O2A	2.708(18)				
Te2B–O5 (×2)	3.285(6)				
$<Te2B–O>_{short}$	**2.143**				
$<Te2B–O>_{long}$	**3.040**				

* *M1* ($Al1_{7/8}Te3_{1/8}$ i.e. *M*1) and Al2 & Te4 ($Al2_{23/24}Te4_{1/24}$ i.e. *M*2) fixed based on EPMA and electron-counting considerations.

Table 5. Bond-valence table for tomiolloite. Values calculated using Gagné & Hawthorne (2015) for all elements except Te, instead using Mills & Christy (2013)

Site	Te1	Te2A	Te2B	*M*1*	*M*2*	S	Σ	Assignment
O1	1.16 (×3↓)			0.57	0.54		**2.27**	O
O2A		1.19 (×0.54↓, ×0.732→)	0.16 (×0.54↓, ×0.268→)				**0.91**	OH
O2B		1.80 (×0.46↓, ×0.732→)	0.26 (×0.54↓, ×0.268→)				**1.39**	OH
O3	0.25 (×3↓)	1.31 (×2↓, ×0.732→)	1.04 (×2↓, ×0.268→)		0.58		**2.07**	O
O4		0.09 (×0.732→)	0.61 (×0.268→)	0.57 (×2→)			**1.36**	O
O5			0.04 (×2↓, ×0.268→)	0.61	0.61		**1.23**	OH
O6				0.61 (×2→)			**1.22**	OH
O7				0.59	0.57		**1.16**	OH
O8				0.44	0.49, 0.42		**1.36**	O
O1S		0.04 (×2↓, ×0.732→)				1.40 (×2↓)	**1.42**	O
O2S						1.43	**1.43**	O
Σ	**4.24**	**4.25**	**2.98**	**3.39**	**3.21**	**4.22**		

***M*1 and *M*2 bond-valences calculated as the ratio of Al^{3+}:Te^{6+} fixed in the structure based on EPMA and electron-counting considerations.

FIGURE CAPTIONS

Figure 1. (a) Optical image of tomiolloite spherical aggregates on semi-translucent tellurite, surrounded by quartz. (b) Tomiolloite 'puffballs' on tellurite showing individual needles, FOV 1 mm. Museums Victoria specimen M55489, photo credit for (b) Brent Thorne.

Figure 2. SEM images of tomiolloite. Bright spots in figure (a) are fragments of tellurite. Museums Victoria specimen M55489.

Figure 3. Spherical aggregates of tomiolloite (white, powdery, spherical aggregates) on the BM 1974,394 mroseite specimen with tellurite (yellow-orange crystals) and mroseite (yellow massive). (a) showing an overview and (b) showing a zoomed view.

Figure 4. IR spectrum of tomiolloite, with key bands labelled.

Figure 5. XPS analysis of Te and S valence in tomiolloite with key peaks labelled. Note that there is some overlap in the S XPS, but the complex signal cannot be generated by one valence alone.

Figure 6. The structure of tomiolloite viewed down *c*. $Te^{4+}O_3$ trigonal pyramids are shown in dark green, $Te^{4+}O_4$ disphenoids in light green, $M1\varphi_6$ octahedra in blue, $M2\varphi_6$ octahedra in grey, S atoms in yellow and O atoms in red.

Figure 7. View of a single crankshaft chain of $M\varphi_6$ octahedra and adorning TeO_n polyhedra.

Figure 8. The split site region showing both Te2 and O2 positions plus nearby strongly-bonded atoms and distances. O3 and O4 shown as displacement ellipsoids at 50% probability; Te2 and O2 are isotropic.

Figure 9. SO_3 (sulfite) trigonal pyramidal groups (as determined by the crystal structure) arranged around the edge of the mesoporous channels of tomiolloite. It is assumed that half of the SO_3 groups have a tetrahedral apex to form SO_4 groups, however the electron density is too low to allow for accurate modelling.

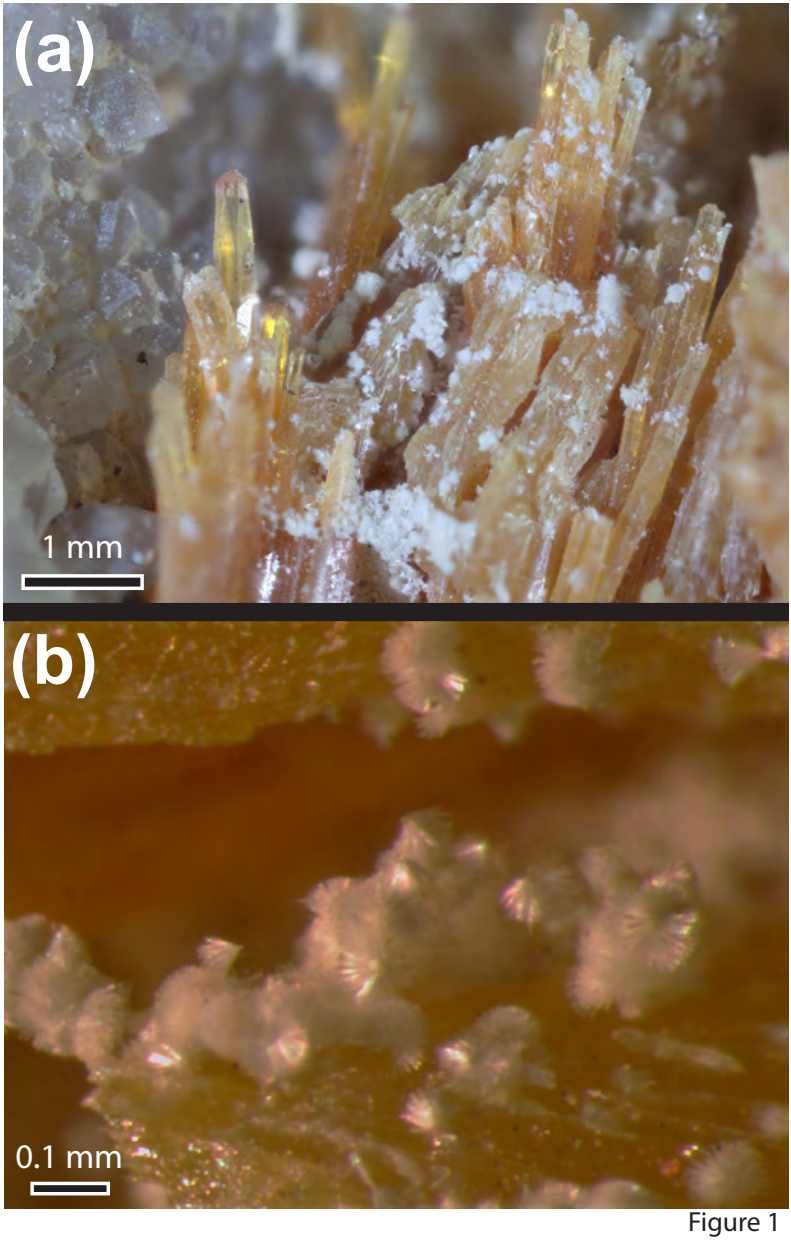

Figure 1

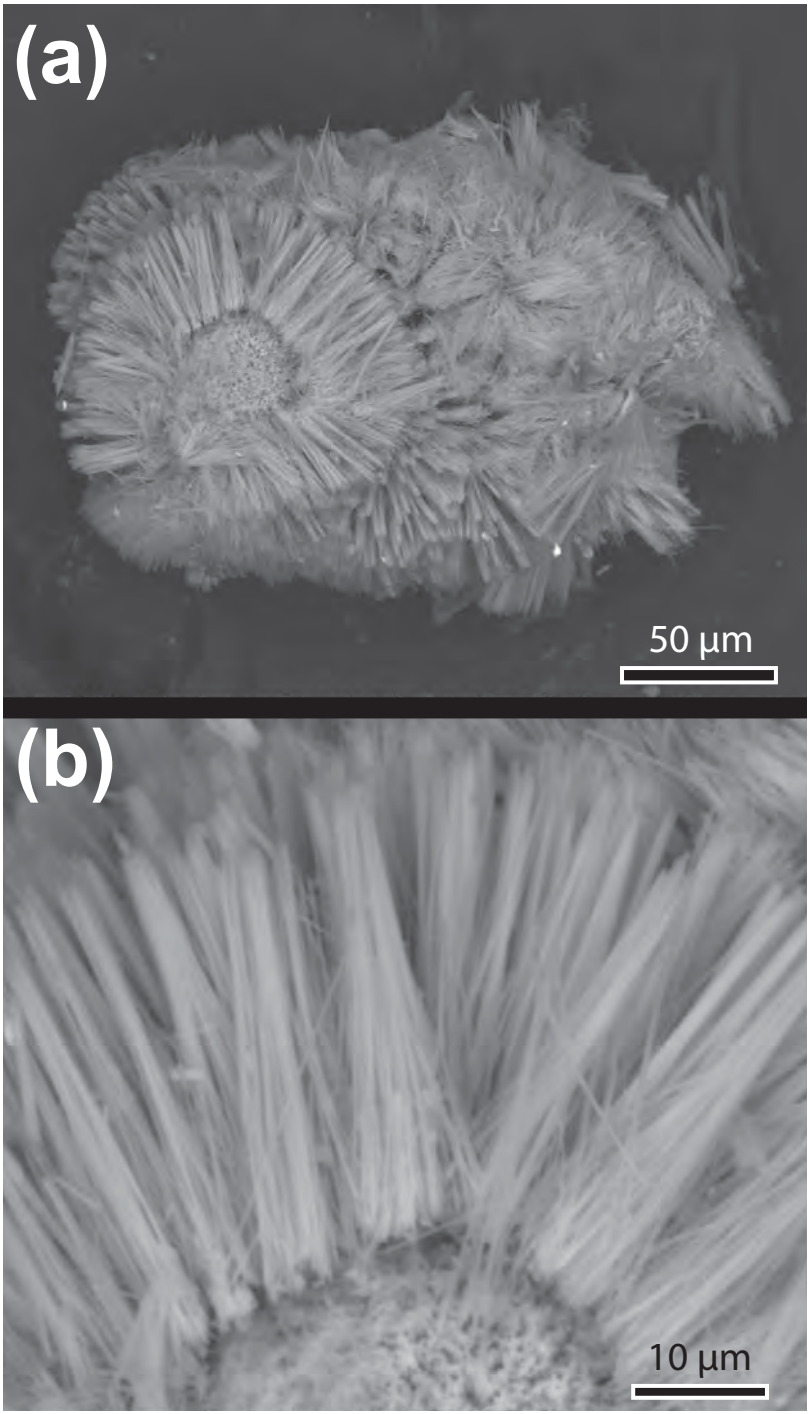

Figure 2

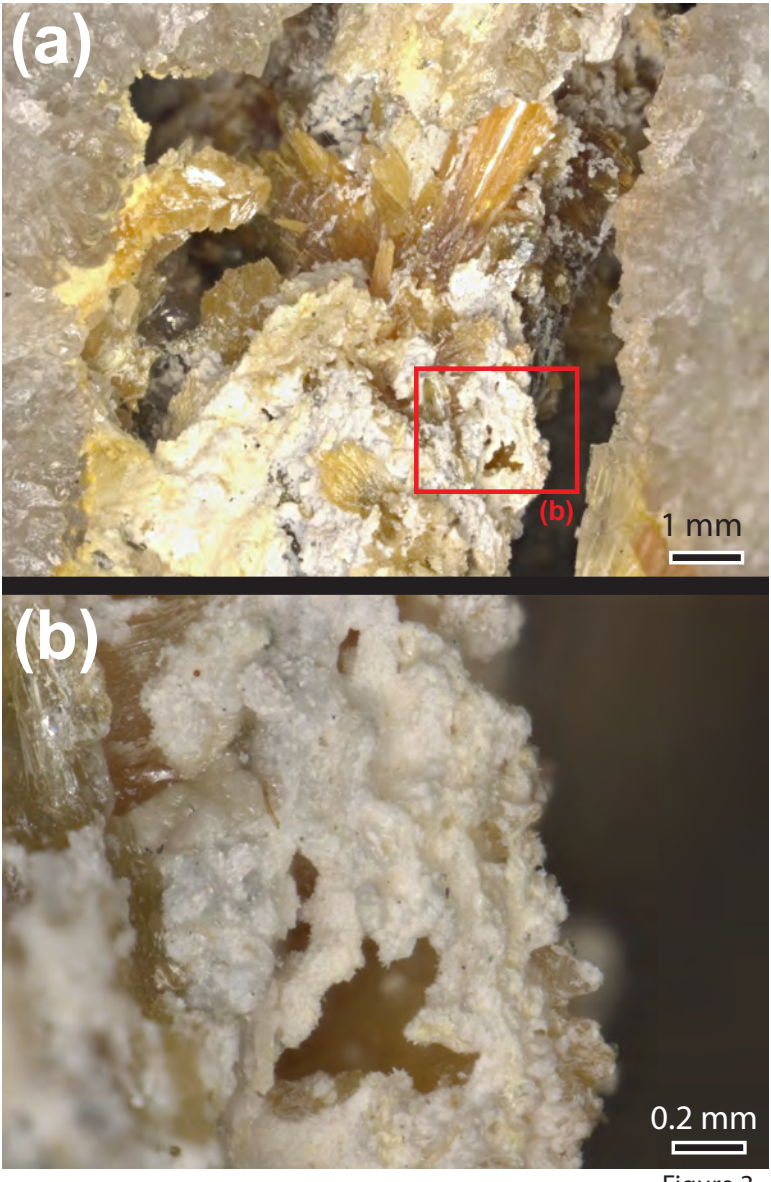

Figure 3

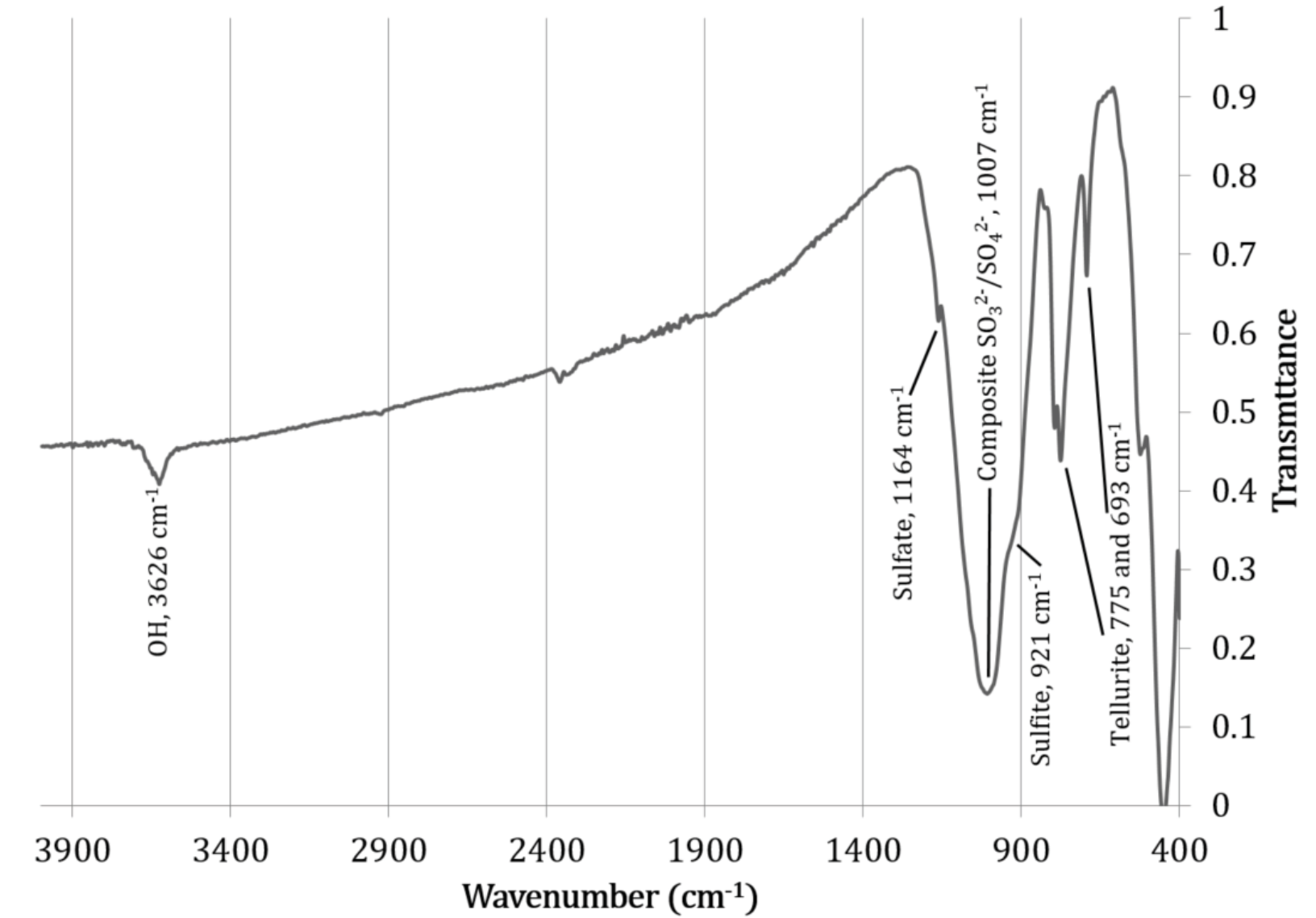
OH, 3626 cm-1
Sulfate, 1164 cm-1
Composite SO3 2-/SO4 2-, 1007 cm-1
Sulfite, 921 cm-1
Tellurite, 775 and 693 cm-1
Transmttance
1
0.9
0.8
0.7
0.6
0.5
0.4
0.3
0.2
0.1
0
3900
3400
2900
2400
1900
1400
900
400
Wavenumber (cm-1)

Figure 4

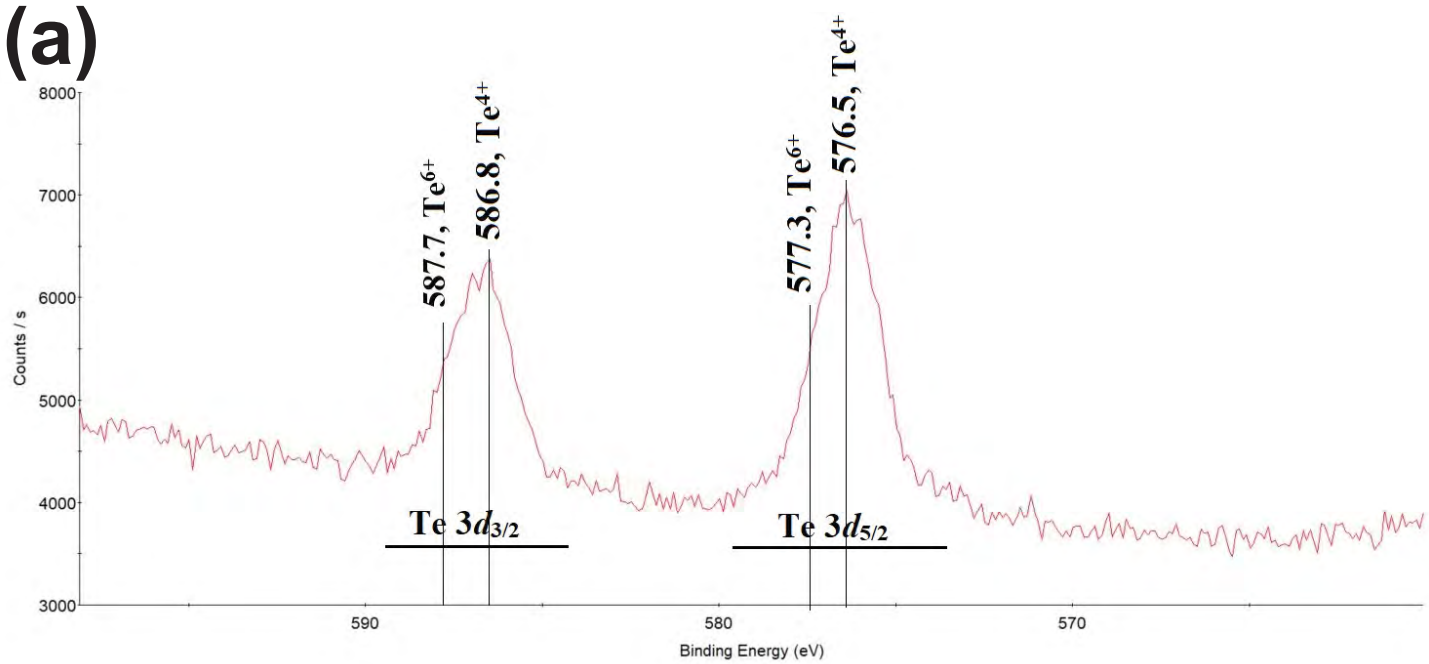
(a)
587.7, Te6+
586.8, Te4+
577.3, Te6+
576.5, Te4+
Te 3d3/2
Te 3d5/2
Counts / s
Binding Energy (eV)

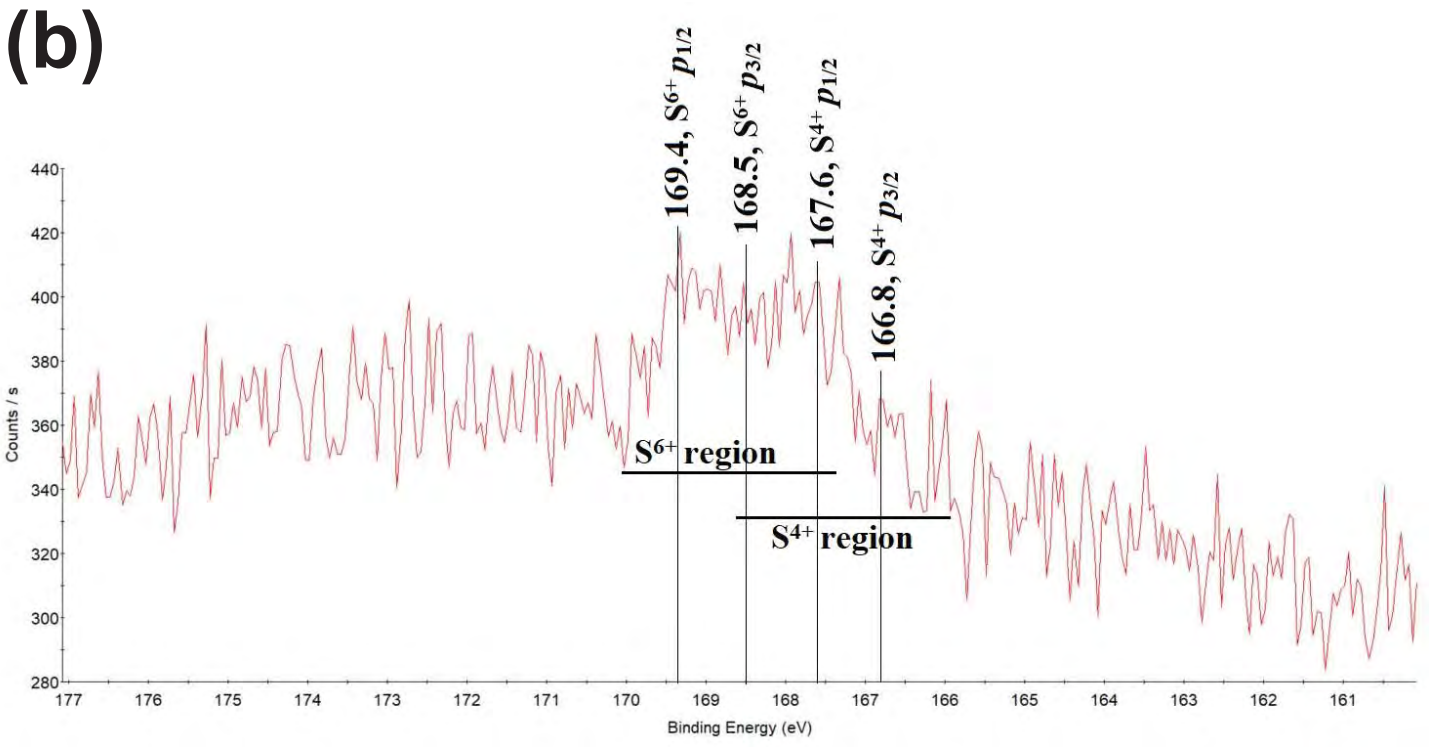
(b)
169.4, S6+ p1/2
168.5, S6+ p3/2
167.6, S4+ p1/2
166.8, S4+ p3/2
S6+ region
S4+ region
Counts / s
Binding Energy (eV)

Figure 5

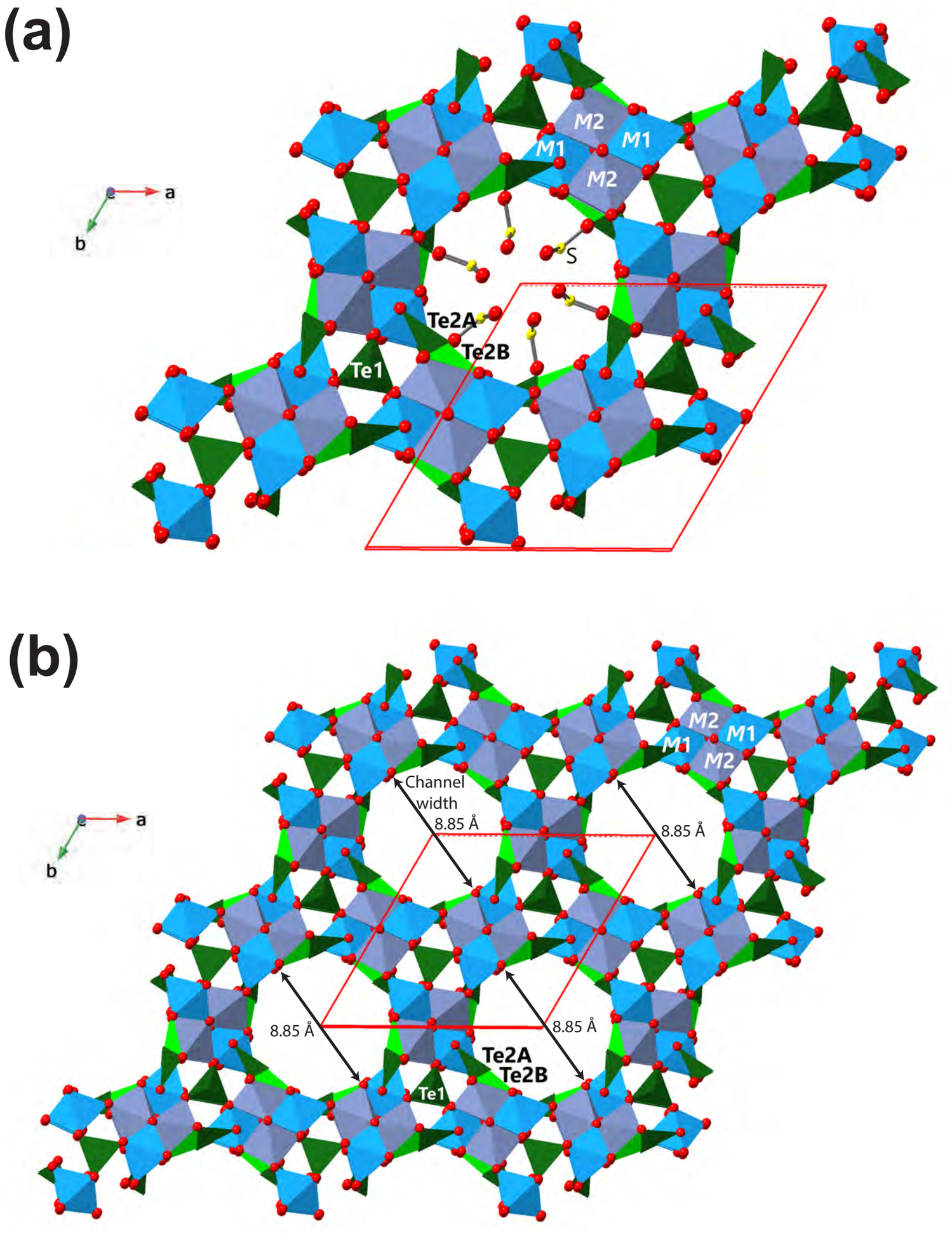
(a)
c
a
b
M2
M1
M1
M2
S
Te2A
Te2B
Te1
(b)
c
a
b
M2
M1
M1
M2
Channel
width
8.85 Å
8.85 Å
8.85 Å
8.85 Å
Te2A
Te2B
Te1

Figure 6

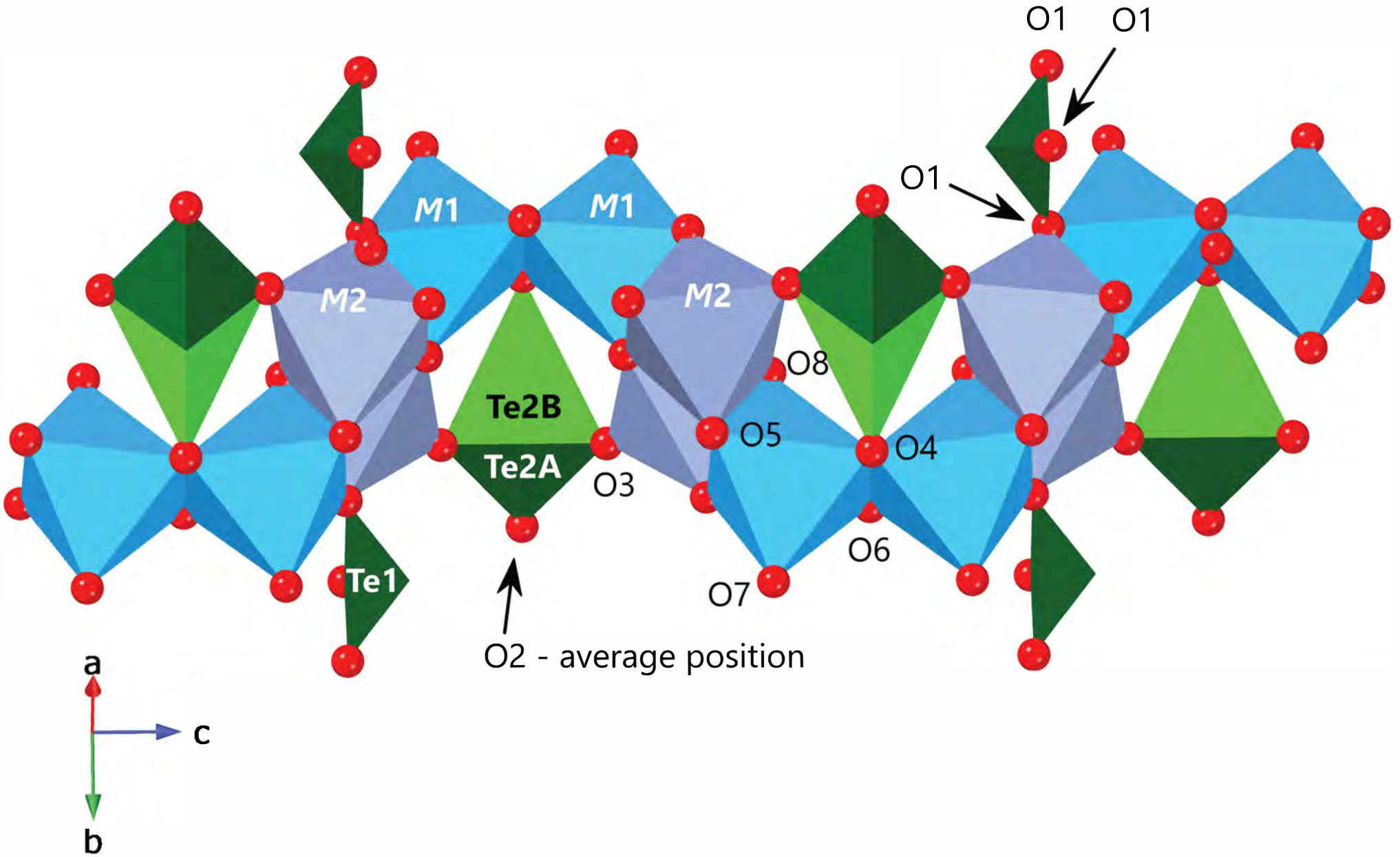
O1
O1
O1
M1
M1
M2
M2
O8
Te2B
Te2A
O3
O5
O4
O6
O7
Te1
O2 - average position
a
c
b

Figure 7

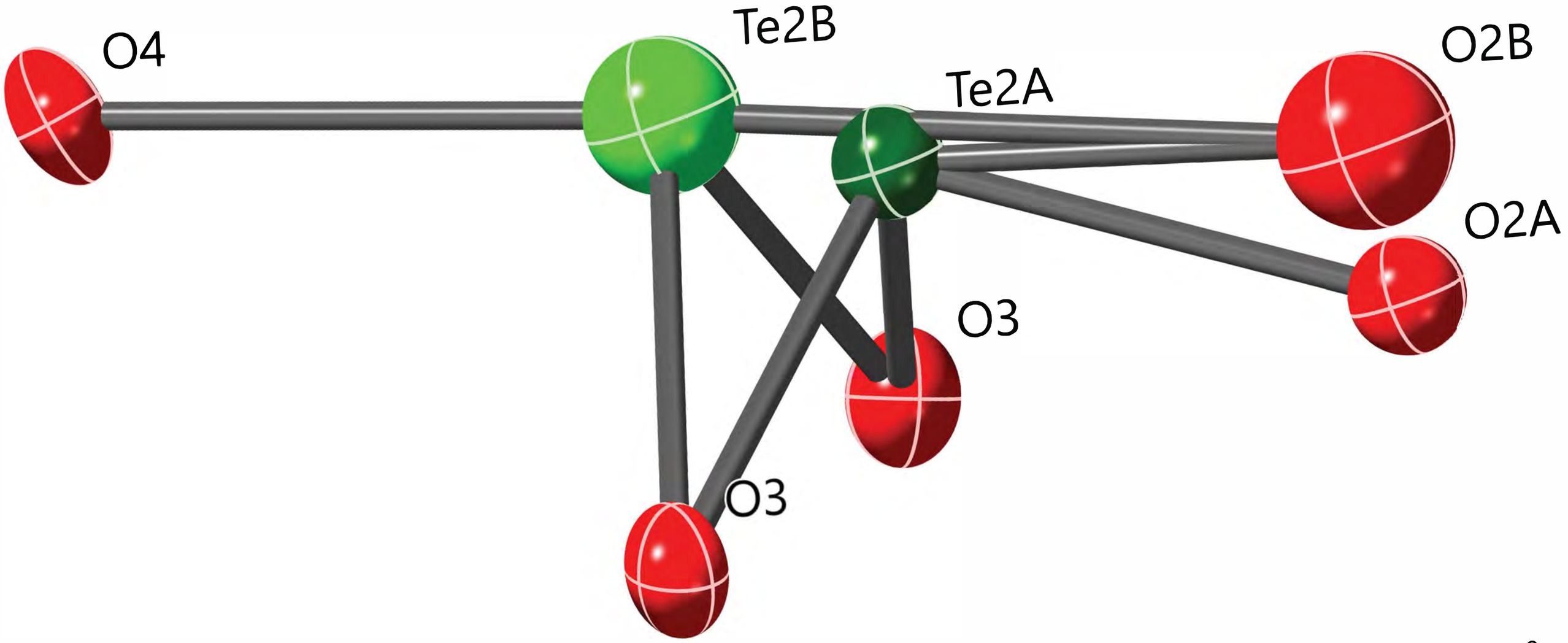

Figure 8

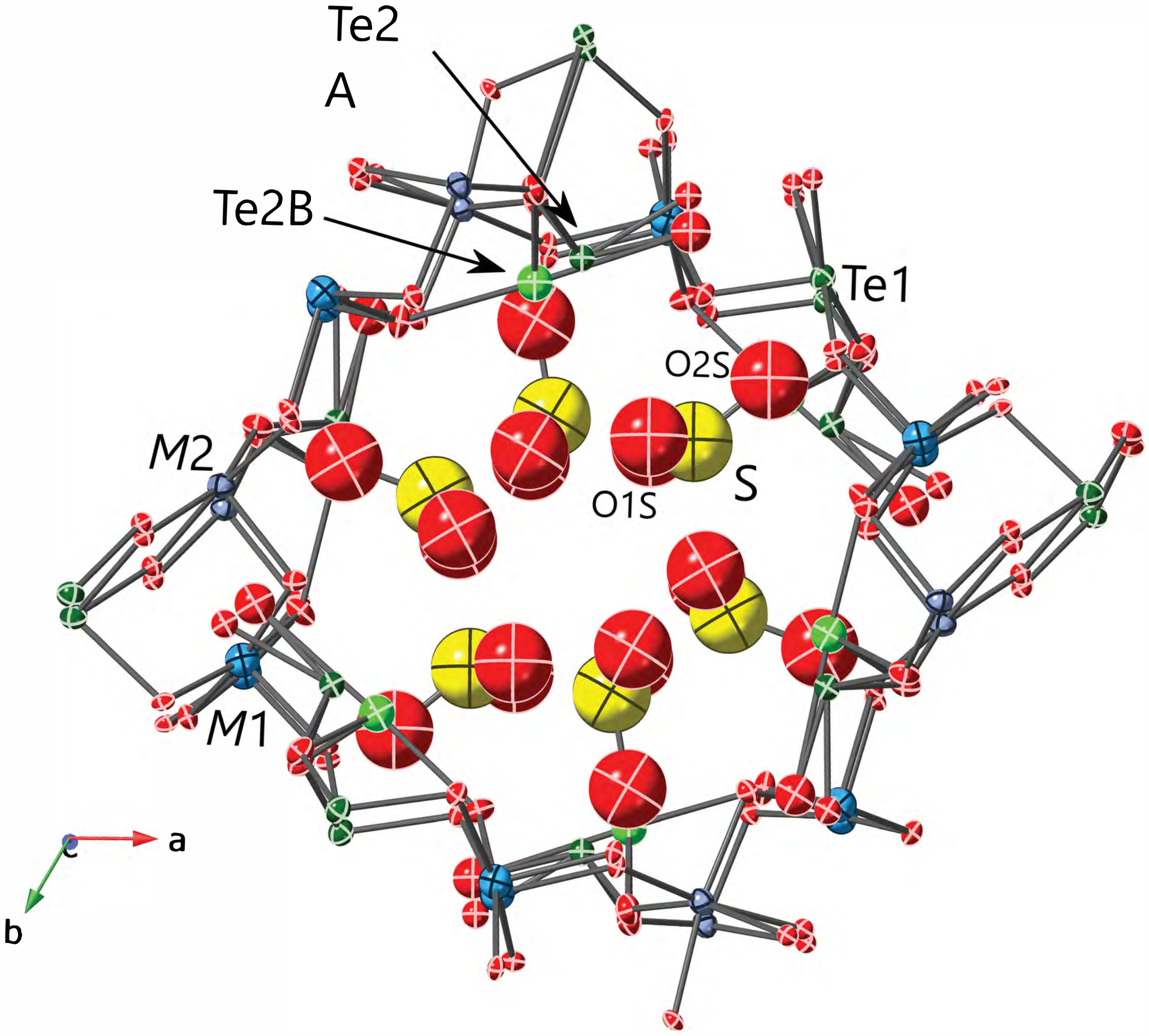

Figure 9